Phase analysis for partially coherent light propagating through an optimized aperture in a synchrotron beamline

Junchao Ren,[a,b] Xiangyu Meng,[c*] Yong Wang,[b,c*] Jiefeng Cao,[c] Junqin Li[c] and Renzhong Tai[b,c*]

[a]Shanghai Institute of Applied Physics, Chinese Academy of Sciences, Zhangheng Road 239, Pudong District, Shanghai 201800, People's Republic of China, [b]University of Chinese Academy of Sciences, Yuquan Road 19, Shijingshan District, Beijing 100049, People's Republic of China, and [c]Shanghai Advanced Research Institute, Chinese Academy of Sciences, Zhangheng Road 239, Pudong District, Shanghai 201800, People's Republic of China. *Correspondence e-mail: mengxiangyu@zjlab.org.cn, wangyong@zjlab.org.cn, tairenzhong@zjlab.org.cn

The mutual optical intensity propagation of partially coherent light through a beamline is calculated for different aperture sizes and positions. The coherence, intensity and phase distribution can be extracted from the mutual optical intensity. The phase distribution depends on the aperture size and position. The results show that the widest flat phase distribution is obtained at the optimized aperture size and position. The aperture plays a more important role for partially coherent light than for incoherent light. The influence of the aperture size and position on the intensity and spot size at the focal plane is also analyzed. A way to obtain a balance between the flat phase distribution area, spot size and intensity for partially coherent light in the beamline is demonstrated.

1. Introduction

The coherence properties of X-rays have been improved since free-electron lasers (Emma *et al.*, 2010; Ishikawa *et al.*, 2012; Hettel, 2014) and diffraction-limited storage rings have developed all over the world (Allaria *et al.*, 2012; Eriksson *et al.*, 2014; Jonge *et al.*, 2014). Many experimental techniques rely on the coherence of synchrotron radiation, such as X-ray lithography (Zhang *et al.*, 2014), coherent diffraction imaging (Whitehead *et al.*, 2009; Vartanyants & Singer, 2010), and X-ray photon correlation spectroscopy (Stephenson *et al.*, 2009; Seaberg *et al.*, 2017). Some experimental techniques require the focal spot not only to have high coherence and high brightness but also to have a large flat phase distribution area, such as plane wave CDI (coherent diffraction imaging) (Whitehead *et al.*, 2009) and biomolecular crystal structure determination (Wolf, 2009; Levantino *et al.*, 2015). Therefore, it is necessary to increase the size of the flat phase distribution area at the focal plane to meet the experimental requirements. Several software packages have been developed for the simulation of partially coherent beams through beamlines, including *SRW* (Chubar, 2014; Chubar *et al.*, 2011), *HYBRID* (Shi *et al.*, 2014), *SHADOW3* (Sanchez del Rio *et al.*, 2011), *PHASE* (Bahrdt *et al.*, 2011) and *XRT* (Sanchez del Rio *et al.*, 2014; Khubbutdinov *et al.*, 2019). Many works have been carried out using these simulation packages for the beamline design. However, the main purpose in the beamline design is focused on high energy resolution, high photon flux and small focal spot. There are few works on improving the flat phase distribution area at the focal plane. Based on statistical optics, we have established a partially coherent X-ray propagation
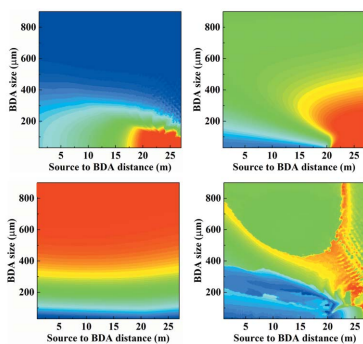
method — the MOI model (Meng *et al.*, 2015, 2017; Ren *et al.*, 2019), which can analyze the mutual optical intensity propagation through the beamline and provide the intensity, coherence, wavevector and phase information at a specified position of the beamline. In this work, we analyze the phase distribution, intensity and spot size of partially coherent light at the focal plane for various sizes and positions of a beam-defining aperture (BDA) in a beamline. The optimized BDA size and position are acquired for the widest flat phase distribution area, intensity and spot size.

2. Theoretical part

2.1. Model description

The MOI model was reported in previous work (Meng *et al.*, 2015, 2017; Ren *et al.*, 2019). We give a summarized description of the model in this paper. The MOI model uses the mutual optical intensity to describe the partially coherent wavefield. The mutual optical intensity represents the distribution of intensity and the correlations between every two points. Its definition can be expressed as (Born & Wolf, 1986)

$$J(x_1, x_2) = \langle u(x_1) u^*(x_2) \rangle = \Gamma_{12} \sqrt{I_1 I_2} \exp(i\varphi_{12}), \quad (1)$$

where J is the mutual optical intensity, x_1 and x_2 are any two points at the source plane, $u(x_1)$ and $u(x_2)$ correspond to their complex amplitudes, I_1 and I_2 correspond to their intensities, respectively; Γ_{12} and φ_{12} are the degree of coherence and the statistically average phase difference between the two points x_1 and x_2, respectively.

The propagation of the mutual optical intensity through free space can be written as (Born & Wolf, 1986; Goodman, 2000)

$$J(w_1, w_2) = \iint J(x_1, x_2) \exp\left[-i \frac{2\pi}{\lambda}(r_2 - r_1)\right]$$
$$\times \frac{\chi(\gamma_1)}{\lambda \sqrt{r_1}} \frac{\chi(\gamma_2)}{\lambda \sqrt{r_2}} \, dx_1 \, dx_2, \quad (2)$$

where λ is the wavelength, x_1 and x_2 are any two points at the source plane, respectively; w_1 and w_2 are any two points at the image plane, respectively; r_1 and r_2 are the x_1-to-w_1 and x_2-to-w_2 distances, respectively; $\chi(\gamma_1)$ and $\chi(\gamma_2)$ are the inclination factors for the inclination angle γ_1 and γ_2, respectively, as shown in Fig. 1.
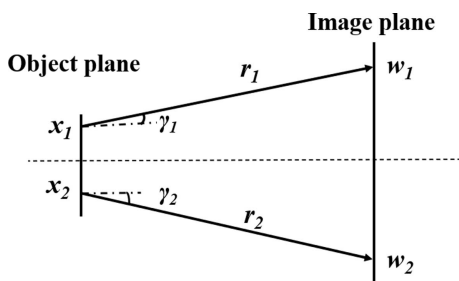
Figure 1
Schematic diagram of the mutual optical intensity propagation through free space.

The mutual optical intensity propagation through free space based on equation (2) is numerically calculated. Firstly, the source plane is divided into many small elements. Each element is small enough to be considered to have full coherence and constant intensity. Using series expansion, r_1 in equation (2) can be written as

$$r_1 = r_{01} - \frac{w_1 x}{r_{01}} + \frac{1}{2} \frac{x^2}{r_{01}} + o(r_1),$$

where r_{01} is the distance between the central points of the two elements x_1 and w_1. The high-order term $o(r_1)$ could be ignored if each element is small enough. Secondly, the propagation of the mutual optical intensity in each element is carried out with the Fraunhofer or Fresnel approximation (Born & Wolf, 1986). Finally, the mutual optical intensity at the image plane can be obtained by summing the contributions of all elements.

The statistically average phase difference from the mutual optical intensity is referred to as phase difference for simplicity, while the phase difference in the fully coherent element is referred to as instantaneous phase difference for distinction. We assume that the instantaneous phase distribution within each element obeys the form of second-order series $\varphi(x) = \varphi_0 + k_0 x + a x^2$, from which we can obtain the in-plane wavevector

$$k(x) = \frac{d\varphi(x)}{dx} = k_0 + 2ax,$$

where k_0 is the in-plane wavevector at the center of each element. The in-plane wavevector is a local and one-point function which depends on only one point. It exists in any partially coherent wavefield since the local area can always be regarded as fully coherent. By integrating the in-plane wavevector in the whole transverse plane, we can obtain the phase distribution of a partially coherent beam. Considering the in-plane wavevector, the mutual optical intensity propagation through free space can be expressed as (Ren *et al.*, 2019)

$$J(w_1, w_2) = \sum \left\{ A(x_2, w_2)^* \left[\sum J(x_1, x_2) A(x_1, w_1) \right] \right\}, \quad (3)$$

where $A(x_1, w_1)$ is the integral of x_1 at the object plane given by

$$A(x_1, w_1) = \int \exp\left[i \frac{2\pi}{\lambda}\left(r_{01} - \frac{w_1 x}{r_{01}} + \frac{1}{2} \frac{x^2}{r_{01}} \right) + i\varphi(x) \right]$$
$$\times \frac{\chi(\gamma_1)}{\lambda \sqrt{r_{01}}} \, dx. \quad (4)$$

2.2. Beamline design

Consider a case where the source is limited by the BDA and focused by an elliptical cylinder mirror, as shown in Fig. 2. The optical setup comes from the BL08U1A beamline at Shanghai Synchrotron Radiation Facility. We take this beamline for example to demonstrate how to optimize the BDA for partially coherent beam. It should be noted that the optimization method should work for similar beamlines. The distance from the source to the elliptical cylinder mirror is 34 m, and
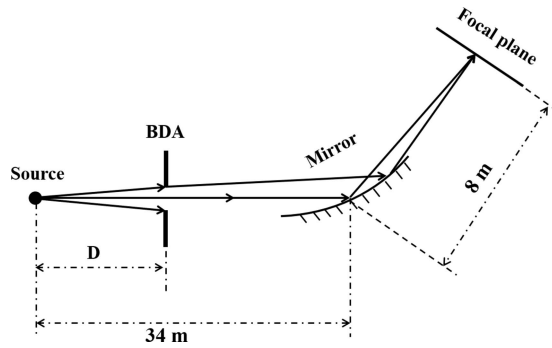
Figure 2
Schematic layout of X-ray propagation through the BDA and elliptical cylinder mirror, where D is the distance from the source to the BDA.

the distance from the mirror to the focal plane is 8 m. For the elliptical cylinder mirror, the meridian focus formula can be expressed as (Born & Wolf, 1986)

$$\frac{1}{r_1} + \frac{1}{r_2} = \frac{2}{R \sin\theta}, \qquad (5)$$

where r_1 and r_2 are the object and image distances, respectively, θ is the grazing incident angle and R is the mirror radii. The BDA is located between the source and the mirror. The mirror has a length of 300 mm and a grazing incident angle of 1.5°. The source is described by a Gaussian model (Starikov & Wolf, 1982; Gori et al., 2001), and the mutual optical intensity at the source plane can be expressed as

$$J_{12} = I_0 \exp\left[-\frac{(x_1 - x_2)^2}{2\chi^2}\right] \exp\left(-\frac{x_1^2 + x_2^2}{4\sigma^2}\right), \qquad (6)$$

where J_{12} is the mutual optical intensity between any two points x_1 and x_2 at the source plane, χ represents the coherence length, σ represents the intensity r.m.s. size, and I_0 is the intensity of the central point. The optical parameters of the source are a wavelength of $\lambda = 2.55$ nm, $\sigma = 153$ μm and $\chi = 109.6$ μm, and the source size is chosen to be 10σ. The global degree of coherence for the source is $G = 0.34$, which is calculated by using the following equation (Vartanyants & Singer, 2010),

$$G = \frac{\int\int |J(x_1, x_2)|^2 \, dx_1 \, dx_2}{\left[\int I(x) \, dx\right]^2}. \qquad (7)$$

We use the MOI model to calculate the propagation of the mutual optical intensity of partially coherent light through the BDA and elliptical cylinder mirror. The intensity, coherence degree, phase distribution and in-plane wavevector can be obtained using the MOI model. A detailed discussion of the MOI model has been given in previous papers (Meng et al., 2015, 2017; Ren et al., 2019).

3. Mutual optical intensity propagation through an ideal mirror

3.1. Mutual optical intensity distribution at the BDA and mirror planes

The mutual optical intensity distribution at the BDA plane is calculated when the source–BDA distance D is 20 m. Then, the intensity, in-plane wavevector and coherence degree are extracted from the mutual optical intensity, as shown in Fig. 3. It should be pointed out that the coherence degree is between any point and the central point at the optical plane in this paper. The r.m.s. beam size $\sigma = 172.03$ μm is obtained by Gaussian fitting of the intensity distribution (black line) in Fig. 3(a). The in-plane wavevector (red line) in Fig. 3(a) shows that the line slope in the central region is 2.59×10^{-5} μm and that the slope at the edges is 1.41×10^{-4} μm. The corresponding spherical wave radii are 95.18 m and 17.53 m. The in-plane wavevector at the BDA plane is determined by the combination of the plane wave of the source and the diffraction of the finite source. The in-plane wavevector in the BDA central region mainly results from the contribution of the plane wave of the source; therefore, the central spherical wave radii of 95.18 m is much larger than the source–BDA
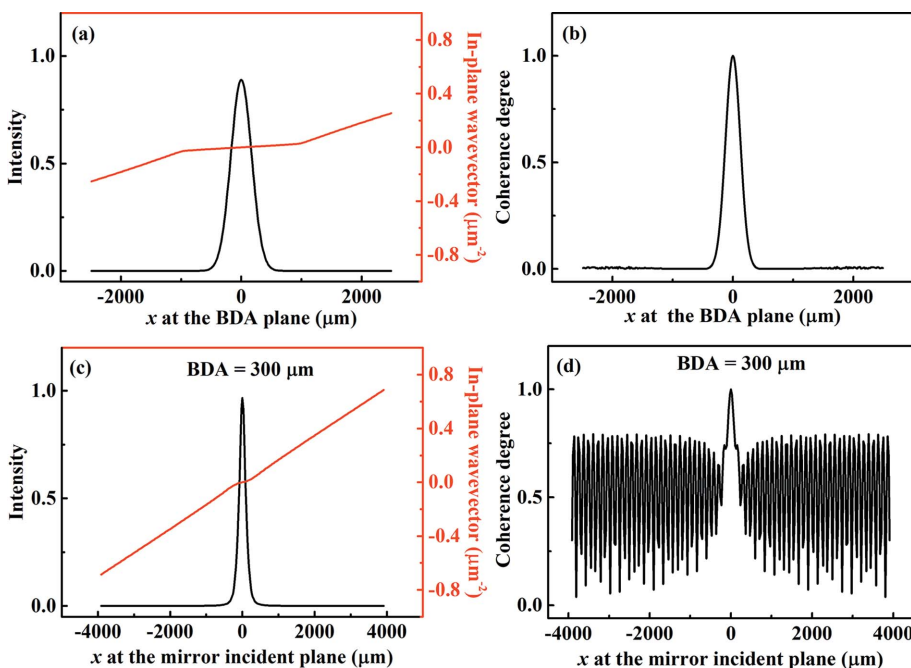
Figure 3
(a) Intensity (black line) and in-plane wavevector (red line) profiles at the BDA plane. (b) Coherence degree profile at the BDA plane. With a BDA size of 300 μm, (c) intensity (black line) and in-plane wavevector (red line) profiles at the mirror incident plane, and (d) coherence degree profile at the mirror incident plane.

distance of 20 m. The in-plane wavevector in the BDA edge regions mainly results from the diffraction of the finite source; therefore, the edge spherical wave radii of 17.53 m is smaller, which is closer to the source–BDA distance. The coherence degree at the BDA plane is an approximately Gaussian distribution, and the coherence length is $\chi = 123$ µm, as shown in Fig. 3(b). According to equation (7), the global degree of coherence at the BDA plane is $G = 0.34$.

We calculated the partially coherent light propagation with a BDA size of 300 µm. The mutual optical intensity distribution at the mirror incident plane, which is perpendicular to the beam and across the mirror center, is acquired. The intensity (black line) and the in-plane wavevector (red line) at the incident plane of the elliptical cylinder mirror are shown in Fig. 3(c). The beam size r.m.s. is $\sigma = 190.7$ µm. The in-plane wavevector consists of three subregions. The slope of the in-plane wavevector in the central region is 5.75×10^{-5} µm^{-2}, and the corresponding spherical wave radii is 42.89 m. The central region wavevector mainly results from the contribution of the source plane wave. Because the BDA size is limited to 300 µm, the BDA can be seen as a secondary source. The in-plane wavevectors in the edge regions mainly result from the

diffraction of the BDA. Therefore, the slope of the in-plane wavevector in the edge regions is 1.78×10^{-4} µm^{-2}, and the corresponding spherical wave radii is 13.81 m, which is close to the BDA–mirror distance of 14 m. The coherence degree at the mirror incident plane is shown in Fig. 3(d). The coherence degree profile has obvious oscillations, which are caused by the diffraction of the BDA. Due to the beam being limited by the BDA, the global degree of coherence at the mirror incident plane increases from 0.34 to 0.54.

3.2. Mutual optical intensity at the focal plane with various BDA size and fixed BDA position

When the source–BDA distance is $D = 20$ m, the mutual optical intensity at the focal plane is analyzed for different BDA sizes. The intensity, in-plane wavevector and coherence degree at the focal plane can be extracted from the mutual optical intensity, as shown in Fig. 4. The BDA size varies from 10 µm to 5000 µm. When the BDA size is 30 µm, the intensity (black line) and the in-plane wavevector (red line) distribution are shown in Fig. 4(a). The spot size r.m.s. at the focal plane is approximately $\sigma = 142.8$ µm. Since the beam size r.m.s. at the
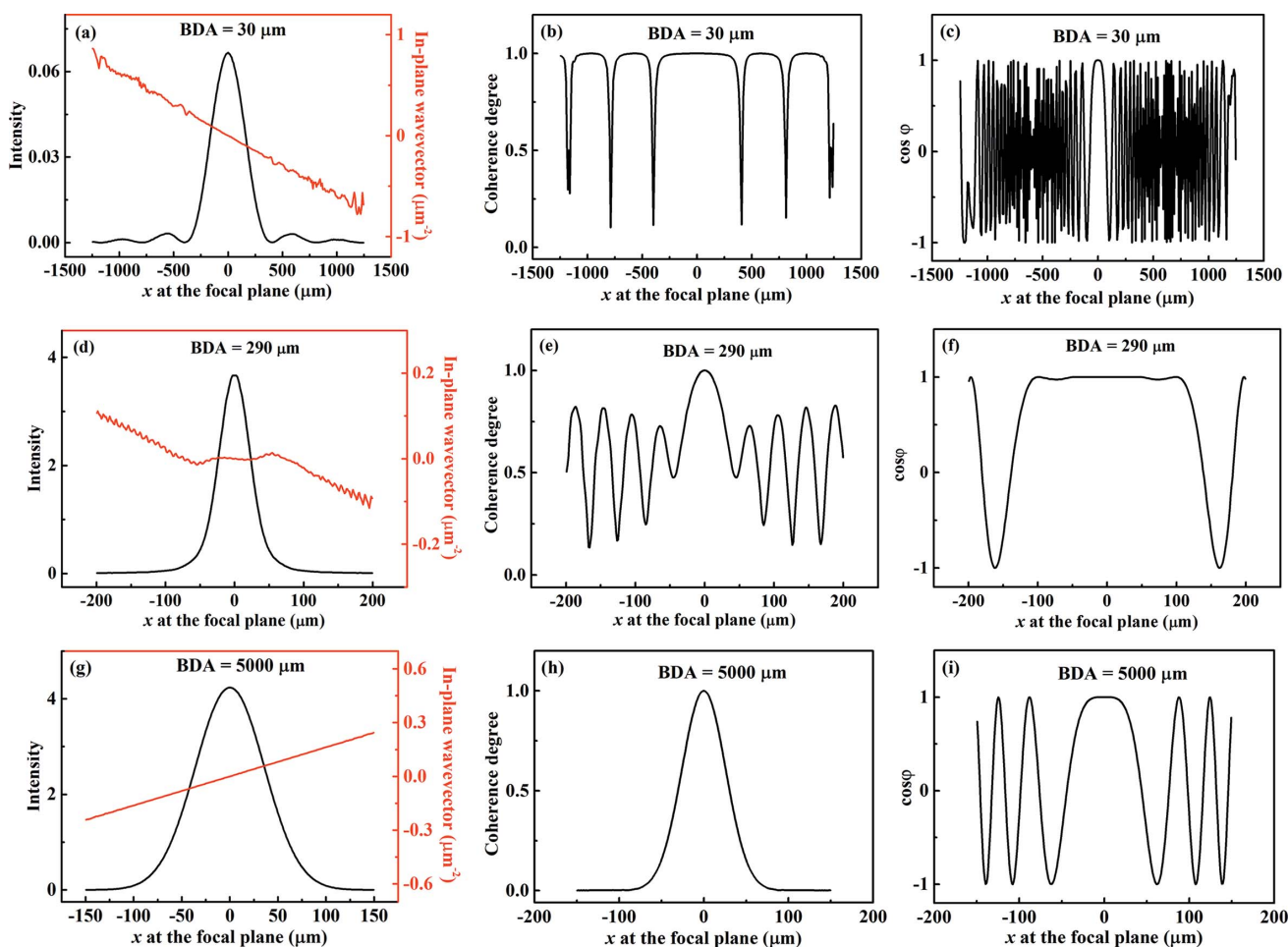
Figure 4
The MOI model is used to calculate the mutual optical intensity distribution at the focal plane. (a, d, g) Intensity (black line) and in-plane wavevector (red line) distributions at the focal plane for various BDA sizes. (b, e, h) Coherence degree and (c, f, i) cos(φ) distributions at the focal plane for various BDA sizes. The BDA sizes are (a, b, c) 30 µm, (d, e, f) 290 µm and (g, h, i) 5000 µm.

BDA plane is $\sigma = 172$ µm, larger than the BDA size of 30 µm, the beam will be limited by the BDA and thus exhibit diffraction at the focal plane. Therefore, the intensity profile has apparent oscillations. The in-plane wavevector profile is approximately a straight line with a slope of -6.08×10^{-4} µm^{-2}, which corresponds to a convergent spherical wave with a radius of 4.05 m. The beam through the BDA can be seen as a secondary source due to the BDA size of 30 µm. Therefore, the image distance changes. According to equation (5), when the object distance r_1 changes from 34 m to 14 m, the image distance r_2 changes from 8 m to 12.05 m, which is coincident with the convergent spherical wave with a radii of 4.05 m. Due to the BDA limiting the X-rays, the coherence degree becomes high, as shown in Fig. 4(b), and the global degree of coherence is 0.99. Fig. 4(c) shows the distribution of the cosine of the phase φ at the focal plane. Assuming the phase with $\cos(\varphi) > 0.95$ is a plane wave in the central region, the plane wave size is 66.45 µm. In this paper, the phase is regarded as a plane wave if $\cos(\varphi) > 0.95$.

The mutual optical intensity with a BDA size of 290 µm at the focal plane is shown in Figs. 4(d), 4(e) and 4(f). The r.m.s. spot size is $\sigma = 22.90$ µm, and the in-plane wavevector has different slopes in the central and edge regions. The limited BDA produces a diffraction effect on the phase distribution at the focal plane. When the optimized BDA size is 290 µm, the diffraction effect of the BDA minimizes the wavevector slope in the central region. The low wavevector slope and high spherical wave radii are -1.33×10^{-4} µm^{-2} and 18.49 m, respectively; therefore, the phase within the small spot of 4σ can be regarded as a plane wave. Fig. 4(f) shows that the phase distribution $\cos(\varphi) \simeq 1$ has a wide range. The plane wave size is 220.61 µm, which is larger than 66.45 µm with a BDA of 30 µm. The image has good coherence, and its global degree of coherence is 0.55.

Due to the beam size r.m.s. of 172 µm at the BDA plane, when the BDA size is 5000 µm, the BDA can be considered to be fully open. The intensity (black line) and in-plane wavevector (red line) distribution at the focal plane are shown in

Table 1
Optical parameters for various transverse planes; the spherical radii are extracted from the wavevector in the central region.

Position	Spot size r.m.s. (µm)	Global degree of coherence	Spherical radii in the central region (m)	Plane wave size with $\cos(\varphi) > 0.95$ (µm)
Source plane	153.00	0.34	∞	–
BDA plane	172.03	0.34	95.18	–
Mirror incident plane	190.70	0.54	42.89	–
Focal plane				
BDA = 30 µm	142.81	0.99	−4.05	66.45
BDA = 200 µm	26.44	0.68	−5.23	71.77
BDA = 290 µm	22.90	0.55	−18.49	220.6
BDA = 500 µm	27.23	0.40	1.71	39.87
BDA = 5000 µm	35.95	30.34	1.52	37.87

Fig. 4(g). The coherence degree and phase distribution are shown in Figs. 4(h) and 4(i). The spot size is $\sigma = 35.95$ µm. The in-plane wavevector distribution is a straight line with a slope of 1.62×10^{-3} µm^{-2}, and the divergent spherical wave radii is 1.52 m. The global degree of coherence is 0.34, and the plane wave size is $\sigma = 37.87$ µm.

The results of the beam size, global degree of coherence, spherical radii in the central region and plane wave size at the focal plane with various BDA size are summarized in the Table 1.

The spot size, in-plane wavevector and plane wave size at the focal plane are calculated for various BDA sizes, as shown in Figs. 5(a), 5(b) and 5(c). When the BDA size is small, the beam at the BDA plane can be seen as a secondary source. Therefore, the spot size is large at the focal plane due to the diffraction effect of the BDA and the defocus aberration. As the BDA size increases, the spot size decreases rapidly. The minimum spot size is $\sigma = 22.90$ µm when the BDA size is 290 µm. As the BDA size increases, the spot size decreases slowly and finally remains at $\sigma = 37.87$ µm.

Figs. 5(b) and 5(c) show the in-plane wavevector slope and plane wave size distribution according to the BDA size. The sign of the slope changes from negative to positive as the BDA size increases. When the BDA size is small, the phase at the focal plane is a divergent spherical wave, and its plane wave is small. As the BDA size increases, the absolute value of the slope becomes small, and the plane wave size becomes large. When the BDA size is 290 µm, the in-plane wavevector slope
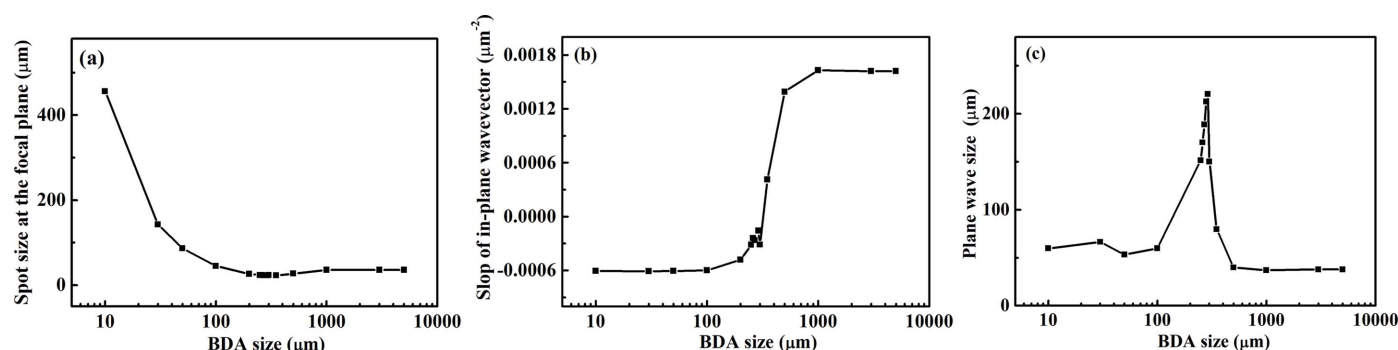
Figure 5
(a) Spot size, (b) in-plane wavevector slope in the central region, and (c) plane wave size at the focal plane as a function of the BDA size. The region with $\cos(\varphi) > 0.95$ is regarded as a plane wave.

is approximately zero, and the plane wave size also reaches the maximum, which indicates that a BDA size of 290 µm is the optimal design for the beamline. With the BDA increasing in size from 290 µm to fully open, the in-plane wavevector slope increases and finally becomes constant. At the same time, the plane wave size decreases rapidly, and the phase changes into a convergent spherical wave. These theoretical results show that one can obtain a small spot, large plane wave and wavevector slope of almost 0 at the focal plane by optimizing the BDA size, while the BDA location cannot be changed. The MOI model can be used to calculate the wavevector and phase distribution, which is important for the optimization of the plane wave at the focal plane.

3.3. Mutual optical intensity at the focal plane with various BDA size and position

In Section 3.2, the plane wave size is optimized by changing the BDA size when the BDA position is fixed. However, the BDA position is also important for beamline design. To optimize the spot size, photon flux and plane wave size at the focal plane, it is necessary to use the MOI model to calculate the partially coherent light propagating through the BDA with various opening size and position.

The plane wave size, photon flux and spot size at the focal plane are calculated for different BDA sizes and positions. Fig. 6(a) shows that the maximum plane wave size has a band-like structure, where the source–BDA distance is between 26 m and 28 m and the BDA size is less than 230 µm. The

plane wave size in the band-like structure ranges from 130 µm to 400 µm, which indicates that the plane wave size at the focal plane can be optimized by selecting an optimum range for the BDA position and size.

The photon flux and spot size with various BDA position and size are shown in Figs. 6(b) and 6(c), respectively. When the BDA position is fixed, as the BDA size increases, the photon flux and spot size become large and small, respectively. To balance the plane wave size, flux and spot size at the focal plane, one can select the upper edge of the band-like structure in Fig. 6(a). Comparing the three images, it is found that when the BDA position and size are 26.2 m and 200 µm, the optimized plane wave size, photon flux and spot size are 365.44 µm, 0.39 and 33.42 µm, respectively. Fig. 6 indicates that the plane wave size, photon flux and spot size at the focal plane depend on the BDA position and size. According to the specific beamline requirement, we can carry out the beamline design by optimizing the BDA position and size to balance the plane wave size, photon flux and spot size.

3.4. Mutual optical intensity distribution along the focal axis

In Section 3.2, when the BDA position is fixed at 20 m, the plane wave size at the focal plane is maximum when optimizing the BDA size to 290 µm. Furthermore, the mutual optical intensity distribution along the focal axis z is calculated. Fig. 7(a) shows that the focal depth for the intensity is large. Due to the diffraction effect of the BDA and the mirror aberration, the focal depth center is located 0.33 m down-
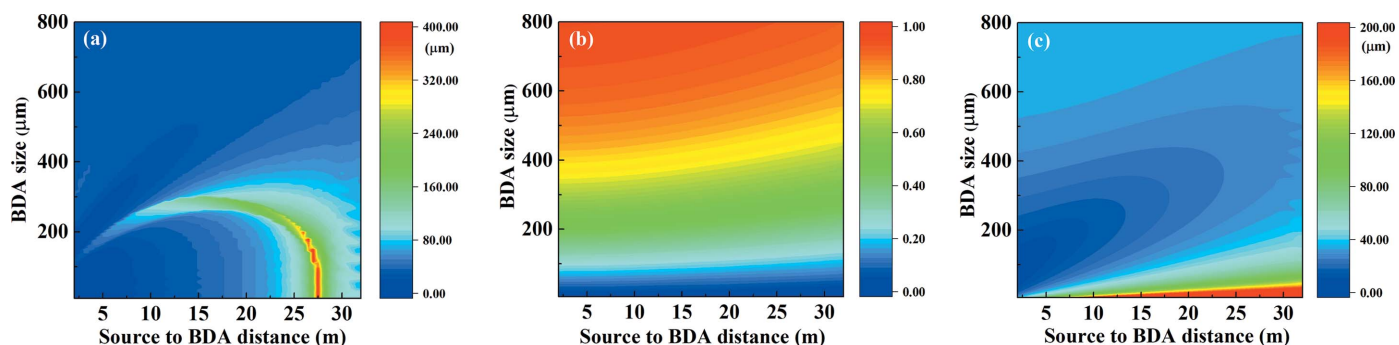
Figure 6
(a) Plane wave size, (b) normalized photon flux and (c) spot size distribution at the focal plane. The horizontal axis is the source–BDA distance, and the vertical axis is the BDA size.
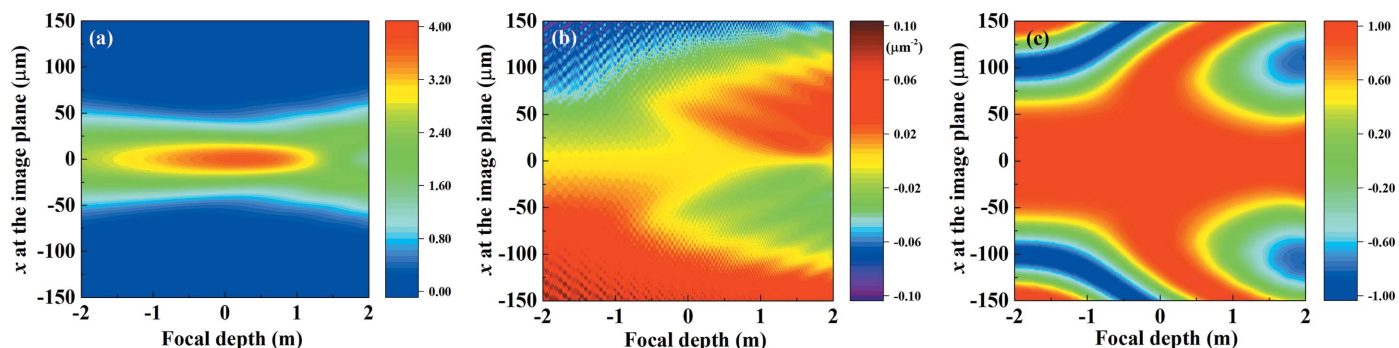
Figure 7
(a) Intensity, (b) in-plane wavevector and (c) phase cosine distribution along the focal axis z.

stream from the focal plane. The distribution of the in-plane wavevector along the focal axis z is shown in Fig. 7(b). The slope of the in-plane wavevector is negative before the focal depth central plane, representing a convergent spherical wave. The slope is positive after the focal depth central plane, representing a divergent spherical wave. The minimum slope for the paraxial in-plane wavevector is located at $z = 0.29$ m. The distribution of the cosine phase $\cos(\varphi)$ along the focal axis z is shown in Fig. 7(c). The maximum plane wave size is located at $z = 0.29$ m. The plane wave size before the focal plane is larger than that after the focal plane. Therefore, if an experiment requires a flat phase at the sample position, the location before the focal plane is a good choice.

4. Mutual optical intensity distribution at the real focal plane

In Section 3, the mutual optical intensity is analyzed at the fixed focal plane, which is located 8 m downstream from the elliptical cylindrical mirror. Analyzing the intensity, wavevector and phase distribution in Fig. 7, the optimum focal spot is located 0.29–0.33 m behind the fixed focal plane. In this section, the real focal plane is calculated for various BDA sizes and positions.

When the BDA is located at 20 m and the size of its opening varies, the distance from the mirror to the real focal plane as a function of the BDA size is shown in Fig. 8(a). The beam at the BDA plane can be seen as a secondary source for a BDA size less than 100 μm. The corresponding image distance is 12 m. According to equation (5), when the object distance r_1 changes from 34 m to 14 m, the image distance r_2 changes from 8 m to 12.05 m. The image distance from the MOI model coincides with the geometrical result. The image distance decreases gradually with increasing BDA size and finally tends to 7 m.

Fig. 8(b) shows the plane wave (black line) and spot size (red line) at the real focal plane. When the BDA size is small, the BDA Fresnel diffraction produces the intensity and plane wave oscillation at the image plane. Therefore, the plane wave size is irregular for a BDA size less than 200 μm. The plane wave size increases with increasing BDA size, and the maximum plane wave size is 248.51 μm with a BDA size of 415 μm. Then, the plane wave size decreases rapidly with

increasing BDA size. The maximum spot size is 36.3 μm with a BDA size of 200 μm. It can be seen that a BDA size of approximately 480 μm is a good choice for the acquisition of a large plane wave and a small focal spot.

Fig. 8(c) shows the normalized photon flux (black line) and global degree of coherence (red line) at the real focal plane. As the BDA size increases, the photon flux increases and the global degree of coherence decreases. When the BDA is fully open, the global degree of coherence is only 0.34.

Similar to Section 3.3, we also calculate the mutual optical intensity at the real focal plane for various BDA sizes and positions.

The real focal distance profile from the mirror in terms of the BDA size and position is shown in Fig. 9(a); it is inversely proportional to the BDA size and proportional to the source–BDA distance. The spot size and photon flux with a various BDA position and size are shown in Figs. 9(b) and 9(c), respectively.

Fig. 9(d) shows that the optimum plane wave size has a band-like structure at the real focal plane, where the source–BDA distance is between 20 m and 24 m, and the BDA size is between 300–500 μm. This result indicates that the plane wave size at the real focal plane can be optimized by selecting an optimum range for the BDA position and size. To balance the plane wave size, flux and spot size at the focal plane, one can select the upper edge of the band-like structure in Fig. 9(d). Comparing these images, it is found that when the BDA position and size are 21 m and 500 μm, respectively, the real focal distance is 6.99 m, and the optimized plane wave size, photon flux and spot size are 260.47 μm, 0.72 and 26.61 μm, respectively.

5. Summary

We simulated the mutual optical intensity propagation of partially coherent light through a beamline for various BDA sizes and positions. The plane wave size, intensity and spot size were acquired at the focal plane and along the focal axis. It was found that the plane wave size at the focal plane has a band-like structure as a function of the BDA size and position, from which one can obtain the maximum plane wave size for the optimized BDA setup. The intensity and spot size distributions as a function of the BDA size and position were also
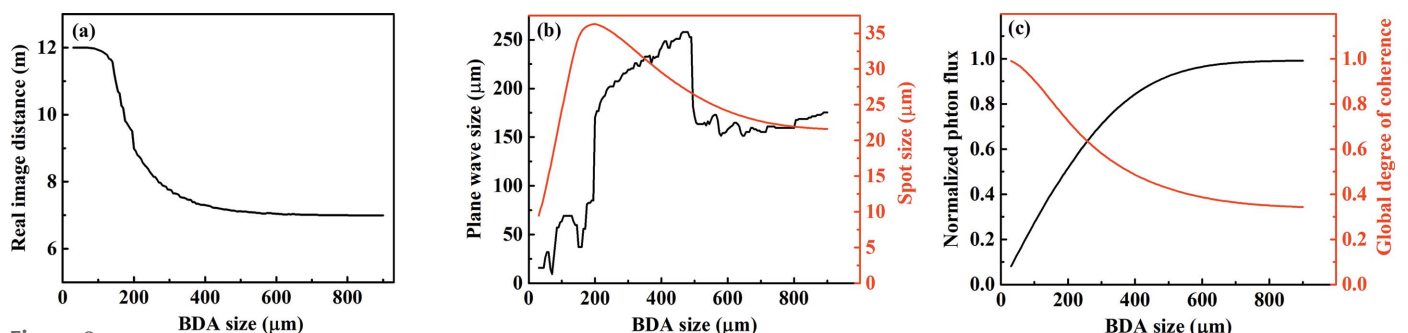
Figure 8
(a) Distance from the mirror to the image plane; (b) plane wave size (black line) and spot size (red line) and (c) normalized photon flux (black line) and global degree of coherence (red line) as a function of the BDA size at the real focal plane.
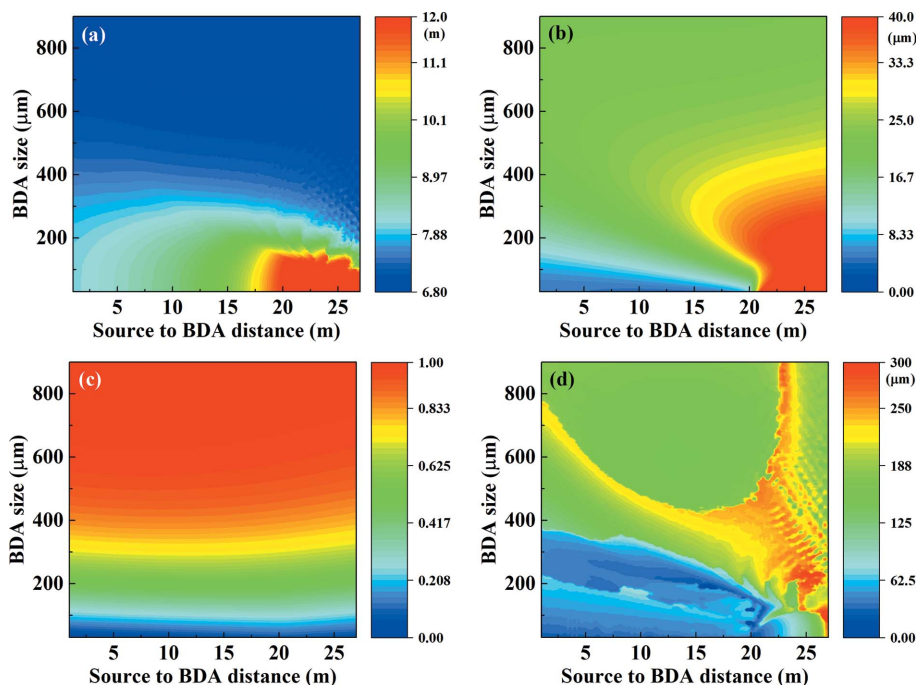
Figure 9
(a) Real focal distance from the mirror, (b) spot size, (c) normalized photon flux and (d) plane wave size distribution. The horizontal axis is the source–BDA distance, and the vertical axis is the BDA size.

acquired. Combining the distributions, we demonstrated a way to obtain a balance between the plane wave size, intensity and spot size by optimizing the BDA setup in a partially coherent beamline, which will be very helpful in the design of beamlines with high coherence.

References

Allaria, E., Appio, R., Badano, L., Barletta, W. A., Bassanese, S., Biedron, S. G., Borga, A., Busetto, E., Castronovo, D., Cinquegrana, P., Cleva, S., Cocco, D., Cornacchia, M., Craievich, P., Cudin, I., D'Auria, G., Dal Forno, M., Danailov, M. B., De Monte, R., De Ninno, G., Delgiusto, P., Demidovich, A., Di Mitri, S., Diviacco, B., Fabris, A., Fabris, R., Fawley, W., Ferianis, M., Ferrari, E., Ferry, S., Froehlich, L., Furlan, P., Gaio, G., Gelmetti, F., Giannessi, L., Giannini, M., Gobessi, R., Ivanov, R., Karantzoulis, E., Lonza, M., Lutman, A., Mahieu, B., Milloch, M., Milton, S. V., Musardo, M., Nikolov, I., Noe, S., Parmigiani, F., Penco, G., Petronio, M., Pivetta, L., Predonzani, M., Rossi, F., Rumiz, L., Salom, A., Scafuri, C., Serpico, C., Sigalotti, P., Spampinati, S., Spezzani, C., Svandrlik, M., Svetina, C., Tazzari, S., Trovo, M., Umer, R., Vascotto, A., Veronese, M., Visintini, R., Zaccaria, M., Zangrando, D. & Zangrando, M. (2012). *Nat. Photon.* **6**, 699–704.

Bahrdt, J., Flechsig, U., Gerhardt, S. & Schneider, I. (2011). *Proc. SPIE*, **8141**, 81410E.

Born, M. & Wolf, E. (1986). *Principles of Optics*, pp. 252–518. Oxford: Pergamon Press.

Chubar, O. (2014). *Proc. SPIE*, **9209**, 920907.

Chubar, O., Chu, Y. S., Kaznatcheev, K. & Yan, H. (2011). *Nucl. Instrum. Methods Phys. Res. A*, **649**, 118–122.

Emma, P., Akre, R., Arthur, J., Bionta, R., Bostedt, C., Bozek, J., Brachmann, A., Bucksbaum, P., Coffee, R., Decker, F. J., Ding, Y., Dowell, D., Edstrom, S., Fisher, A., Frisch, J., Gilevich, S., Hastings, J., Hays, G., Hering, P., Huang, Z., Iverson, R., Loos, H., Messerschmidt, M., Miahnahri, A., Moeller, S., Nuhn, H. D., Pile, G., Ratner, D., Rzepiela, J., Schultz, D., Smith, T., Stefan, P., Tompkins, H., Turner, J., Welch, J., White, W., Wu, J., Yocky, G. & Galayda, J. (2010). *Nat. Photon.* **4**, 641–647.

Eriksson, M., van der Veen, J. F. & Quitmann, C. (2014). *J. Synchrotron Rad.* **21**, 837–842.

Goodman, J. W. (2000). *Statistical Optics*, p. 198. Wiley Classics Library Edition.

Gori, F., Santarsiero, M., Piquero, G., Borghi, R., Mondello, A. & Simon, R. (2001). *J. Opt. A: Pure Appl. Opt.* **3**, 1–9.

Hettel, R. (2014). *J. Synchrotron Rad.* **21**, 843–855.

Ishikawa, T., Aoyagi, H., Asaka, T., Asano, Y., Azumi, N., Bizen, T., Ego, H., Fukami, K., Fukui, T., Furukawa, Y., Goto, S., Hanaki, H., Hara, T., Hasegawa, T., Hatsui, T., Higashiya, A., Hirono, T., Hosoda, N., Ishii, M., Inagaki, T., Inubushi, Y., Itoga, T., Joti, Y., Kago, M., Kameshima, T., Kimura, H., Kirihara, Y., Kiyomichi, A., Kobayashi, T., Kondo, C., Kudo, T., Maesaka, H., Maréchal, X. M., Masuda, T., Matsubara, S., Matsumoto, T., Matsushita, T., Matsui, S., Nagasono, M., Nariyama, N., Ohashi, H., Ohata, T., Ohshima, T., Ono, S., Otake, Y., Saji, C., Sakurai, T., Sato, T., Sawada, K., Seike, T., Shirasawa, K., Sugimoto, T., Suzuki, S., Takahashi, S., Takebe, H., Takeshita, K., Tamasaku, K., Tanaka, H., Tanaka, R., Tanaka, T., Togashi, T., Togawa, K., Tokuhisa, A., Tomizawa, H., Tono, K., Wu, S., Yabashi, M., Yamaga, M., Yamashita, A., Yanagida, K., Zhang, C., Shintake, T., Kitamura, H. & Kumagai, N. (2012). *Nat. Photon.* **6**, 540–544.

Jonge, M. D. de, Ryan, C. G. & Jacobsen, C. J. (2014). *J. Synchrotron Rad.* **21**, 1031–1047.

Khubbutdinov, R., Menushenkov, A. P. & Vartanyants, I. A. (2019). *J. Synchrotron Rad.* **26**, 1851–1862.

Levantino, M., Yorke, B. A., Monteiro, D. C., Cammarata, M. & Pearson, A. R. (2015). *Curr. Opin. Struct. Biol.* **35**, 41–48.

Meng, X., Shi, X., Wang, Y., Reininger, R., Assoufid, L. & Tai, R. (2017). *J. Synchrotron Rad.* **24**, 954–962.

Meng, X., Xue, C., Yu, H., Wang, Y., Wu, Y. & Tai, R. (2015). *Opt. Express*, **23**, 29675–29686.

Ren, J., Wang, Y., Meng, X., Shi, X., Assoufid, L. & Tai, R. (2019). *J. Synchrotron Rad.* **26**, 1198–1207.

Sanchez del Rio, M., Canestrari, N., Jiang, F. & Cerrina, F. (2011). *J. Synchrotron Rad.* **18**, 708–716.

Sanchez del Rio, M., Chubar, O., Klementiev, K. & Chernikov, R. (2014). *Proc. SPIE*, **9209**, 92090A.

Seaberg, M. H., Holladay, B., Lee, J. C. T., Sikorski, M., Reid, A. H., Montoya, S. A., Dakovski, G. L., Koralek, J. D., Coslovich, G., Moeller, S., Schlotter, W. F., Streubel, R., Kevan, S. D., Fischer, P.,

Fullerton, E. E., Turner, J. L., Decker, F. J., Sinha, S. K., Roy, S. & Turner, J. J. (2017). *Phys. Rev. Lett.* **119**, 067403.

Shi, X., Reininger, R., Sanchez del Rio, M. & Assoufid, L. (2014). *J. Synchrotron Rad.* **21**, 669–678.

Starikov, A. & Wolf, E. (1982). *J. Opt. Soc. Am.* **72**, 923–928.

Stephenson, G. B., Robert, A. & Grübel, G. (2009). *Nat. Mater.* **8**, 702–703.

Vartanyants, I. A. & Singer, A. (2010). *New J. Phys.* **12**, 035004.

Whitehead, L. W., Williams, G. J., Quiney, H. M., Vine, D. J., Dilanian, R. A., Flewett, S., Nugent, K. A., Peele, A. G., Balaur, E. & McNulty, I. (2009). *Phys. Rev. Lett.* **103**, 243902.

Wolf, E. (2009). *Phys. Rev. Lett.* **103**, 075501.

Zhang, P., Yang, S., Wang, L., Zhao, J., Zhu, Z., Liu, B., Zhong, J. & Sun, X. (2014). *Nanotechnology*, **25**, 245301.